




## Effect of electrostatic forcing on coaxial two-fluid atomization

Rodrigo Osuna-Orozco <sup>1,\*</sup>, Nathanael Machicoane <sup>2</sup>, Peter D. Huck <sup>3</sup> and Alberto Aliseda<sup>1</sup>

<sup>1</sup>*Department of Mechanical Engineering, University of Washington, Seattle, Washington 98195, USA*

<sup>2</sup>*Université Grenoble Alpes, CNRS, Grenoble INP, LEGI, 38000 Grenoble, France*

<sup>3</sup>*Department of Mechanical and Aerospace Engineering, George Washington University, Washington, DC 20052, USA*



(Received 8 October 2021; accepted 14 June 2022; published 11 July 2022)

We present an experimental investigation of the electrostatically assisted primary atomization in a coaxial gas-liquid jet. Shadowgraphy imaging reveals the primary breakup dynamics and allows for a semiquantitative assessment of the resulting droplet characteristics. We describe the statistics of the liquid core in terms of the probability distributions of its length, the spray angle, and the virtual origin. A strong axial electric field reduces the liquid core length over a wide range of gas-to-liquid momentum ratios, whereas a predominantly radial electric field influences the atomization process weakly. We characterize the primary breakup dynamics in terms of two frequencies associated with the liquid mass: the flapping frequency and the droplet-shedding frequency. Using a combination of proper orthogonal decomposition and Fourier transforms in time and space, we derive empirical dispersion relations. Observations of the initial interfacial instabilities' growth reveal shorter wavelengths and higher growth rates in the presence of a strong axial electric field. This enhanced growth of the interfacial instabilities is consistent with a mechanism whereby Maxwell's stresses drive liquid ligaments out radially across the high-speed annular gas jet, thus improving the momentum transfer between the two phases and enhancing the breakup process (producing smaller final droplet sizes). These results illustrate the importance of the electric field configuration to assist two-fluid coaxial atomization and establish electrostatic forcing as a potential feedback control input.

DOI: [10.1103/PhysRevFluids.7.074301](https://doi.org/10.1103/PhysRevFluids.7.074301)

### I. INTRODUCTION

Multiphysics control of atomization is a promising new area of research that could result in more robust and versatile atomizers that can produce the desired range of droplets under very diverse operating conditions, enabling their use in applications that require the atomization process to operate within tight bounds under the influence of a changing environment and external perturbations (like what may occur in the combustion chamber of a jet engine on board an aircraft or in a coating process with heat and mass transfer and phase change). Although a very wide range of atomizers have been designed for various applications, the spray characteristics produced are typically determined by the design itself and offer limited controllability in the presence of perturbations. These could be environment changes or variability of the liquid properties, the injected flow rate, etc., leading to fluctuations in the produced droplet size and number density that could drift outside acceptable spray properties. The development of robust and versatile closed-loop control strategies for atomization remains a fundamental challenge, and including multiphysics actuation

---

\*roo3@uw.edu

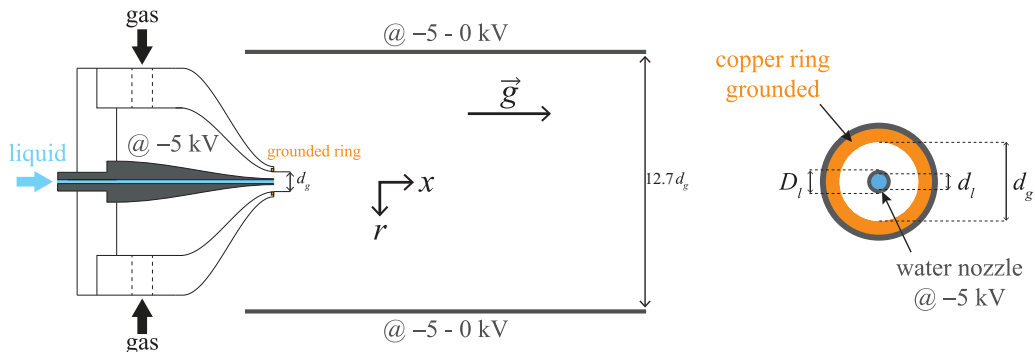


FIG. 1. Side cut and front view of the atomizer showing relevant dimensions;  $d_l$  is the liquid nozzle inner diameter,  $D_l$  is the liquid nozzle outer diameter, and  $d_g$  is the gas nozzle inner diameter. The metallic plates are  $8 \times 8$  and  $5$  in. apart. The gas nozzle is made of plastic whereas the liquid nozzle is made of aluminum.

(e.g., electrostatics, acoustics, swirl, etc.) may offer a possible solution for this fundamental problem or for specific applications [1–4].

Although both electrostatic and coaxial atomization have each been studied extensively [5–11], atomization that combines both a high-speed coaxial gas jet and electrostatic forces remains relatively unexplored, especially at high gas-to-liquid momentum ratios [12,13]. Most of the work exploring the combination of electrostatic atomization and a coflowing gas has been done from the perspective of the electro-flow focusing technique introduced by Gañán-Calvo *et al.* [14,15]. This technique has seen very fruitful applications for mass spectrometry [16,17] and in the context of microfluidics involving two liquid phases [18–20]. Allaf-Akbari and Ashgriz [21] explored atomization regimes of electrospray in gaseous cross flow, involving either stable or unstable Taylor cone jets where the main atomization mechanism is electrostatic. Notably, research has focused mostly on situations in which the mass flow rate and Reynolds number of the liquid jet are very small (amenable to the aforementioned applications). The current work explores a substantially different regime where atomization is mostly achieved by the aerodynamic stresses at the interface. This regime of electrostatically assisted coaxial atomization is useful to introduce additional actuation capabilities for control of two-fluid atomization.

In this paper, we present experimental observations of the primary breakup of an electrically charged laminar liquid jet by a turbulent coaxial gas flow and an external electric field. Section II describes the experimental setup and experimental methods. Section III summarizes the results, and Sec. IV presents the discussion of the results. Section V contains the conclusions.

## II. METHODS

### A. Atomizer

We studied the atomization of an electrically charged laminar liquid jet exposed to a turbulent coaxial gas stream for gas-to-liquid momentum ratios ranging from 1 to 25. We define the momentum ratio  $M$  as the ratio of the dynamic pressure of the gas to that of the liquid,  $M = \rho_g U_g^2 / \rho_l U_l^2$ , where  $\rho$  is the density,  $U$  is the mean velocity computed as the volume flow rate divided by the cross-sectional area of the nozzle, and the subscripts indicate the gas and liquid phases. The working liquid was reverse-osmosis purified water with a conductivity of  $3 \mu\text{S}/\text{cm}$ , and the gas was standard air. The canonical coaxial atomizer (see Fig. 1) used for this study is open source [22]. The design, fabrication, and operational aspects were described in detail in a previous work [23]. Figure 1 shows a schematic of the atomization setup.

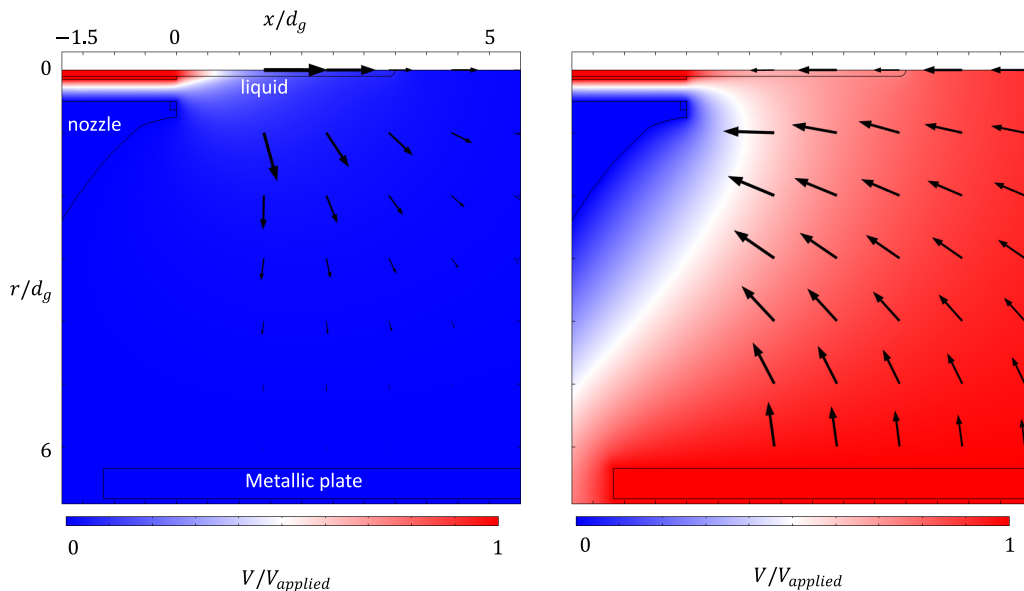


FIG. 2. Finite-element method simulation illustrating the voltage and electric field lines for the two cases considered: grounded plates (left) and charged plates (right). Notice that when the plates are grounded, the electric field is predominantly radial, whereas when the plates are charged, the electric field has a strong axial component over a broader region.

### B. Electric field geometry

A strong electric field approaching the dielectric strength of air was established by connecting the metal liquid nozzle to a high-voltage power supply at an electric potential of  $-5$  kV and grounding a copper ring at the perimeter of the gas nozzle (see Fig. 1). Thus, the liquid droplets issuing from the atomizer were negatively charged. To shape the geometry of the electric field in the atomization region, a pair of metallic plates running along the spray axis was either grounded or set to a potential of  $-5$  kV (equal to that of the liquid nozzle). Electrical arcing was observed to occur for all conditions when the voltage reached  $-6$  kV.

Figure 2 illustrates the geometry of the electric field in the configurations explored, as obtained from finite-element simulations. When the plates are grounded, the electric field is predominantly radial (Fig. 2, left), whereas when the plates are at the same potential as the liquid nozzle, the electric field has a large axial component (Fig. 2, right).

For these simulations we assumed a straight liquid jet of a length that's relevant to the range of  $M$  studied. The nondimensional group describing the ratio of electrostatic to inertial forces, the electrical Euler number [12], was estimated to be  $Eu = \epsilon_g E_0^2 / \rho_l U_l^2 \approx 10^{-2}$ , where  $\epsilon_g$  is the permittivity of air and the electric field strength  $E_0$  is given by the voltage drop and the distance between the nozzle and the grounded ring. For all the explored conditions, the momentum ratio was at least two orders of magnitude larger than the electrical Euler number, indicating a dominance of the aerodynamic shear forces over the electrostatic forces.

### C. High-speed imaging

High-speed shadowgraphy imaging with a temporal resolution of  $100 \mu\text{s}$  (10 000 frames/s) was used to identify the liquid core and the resulting droplets. The spatial resolution of the imaging was  $91.3$  or  $27.3 \mu\text{m}/\text{pixel}$ , where the lower resolution was utilized for the lower momentum ratio conditions. Image postprocessing identified the presence of liquid along the line of sight of the

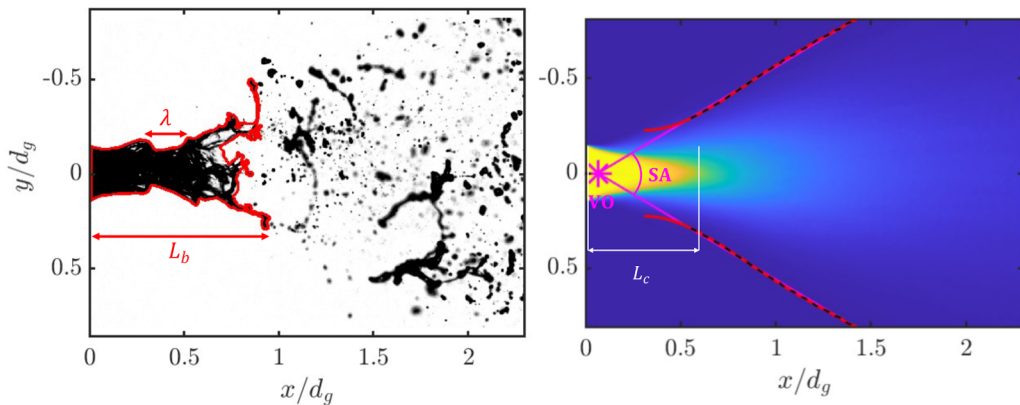


FIG. 3. Metrics used to characterize the spray morphology. Wavelength  $\lambda$  of interfacial instabilities and instantaneous liquid intact length shown for a single snapshot (left). Metrics derived from the mean intensity field (right) include the virtual origin (VO), the spreading angle (SA), and the liquid core length.

camera following methods described previously [24]. Figure 3 illustrates the liquid core as delineated digitally from the images, with the intact length  $L_b$  defined as the farthest distance downstream from the nozzle where there is liquid continuously connected to the issuing liquid jet. Similarly, the resulting droplet population was characterized based on identification of approximately circular objects in the image. Only detected objects whose perimeter was less than  $2\pi$  times their equivalent diameter (where the equivalent diameter is computed from the objects' projected area on the image) are used in the analysis as valid droplets.

The spray angle and virtual origin (the point where linear projections of the points defining the width of the jet converge; see Fig. 3) were obtained following the method proposed by us in a previous work [24]. The liquid core length was obtained from the mean image intensity map using a threshold to identify the region always occupied by liquid.

The entrainment speed  $u_e$  and wavelength  $\lambda$  of the initial interfacial instabilities were computed by tracking local maxima of the gas-liquid interface radial position. The growth rate of the instabilities  $\dot{\xi}/\xi$  (where  $\xi$  is the radial position of the interface relative to the unperturbed state) was approximated based on the relation proposed by Villermaux [25,26] [Eq. (1)]. The velocities were estimated using tracks of local maxima (similar to what was done in previous work [27]) that were at least four frames long and could be fitted with a quadratic expression (assuming nearly constant acceleration) with  $R^2 > 0.99$ :

$$u_e \approx \lambda \frac{\dot{\xi}}{\xi}. \quad (1)$$

Proper orthogonal decomposition (POD) from the images was performed by an implementation of the singular value decomposition analysis. For the purpose of identifying the dynamics of the liquid core, POD was applied to the images after applying a mask that removed drops and ligaments. To derive the empirical dispersion relation, a two-dimensional Fourier transform on all POD modes and a one-dimensional Fourier transform on their corresponding time vectors were performed. For robustness, a power spectral density (PSD)-weighted mean of the temporal frequency and spatial wavelength was computed. Thus, we obtained unique frequency-wavelength pairs for each POD mode (Fig. 4).

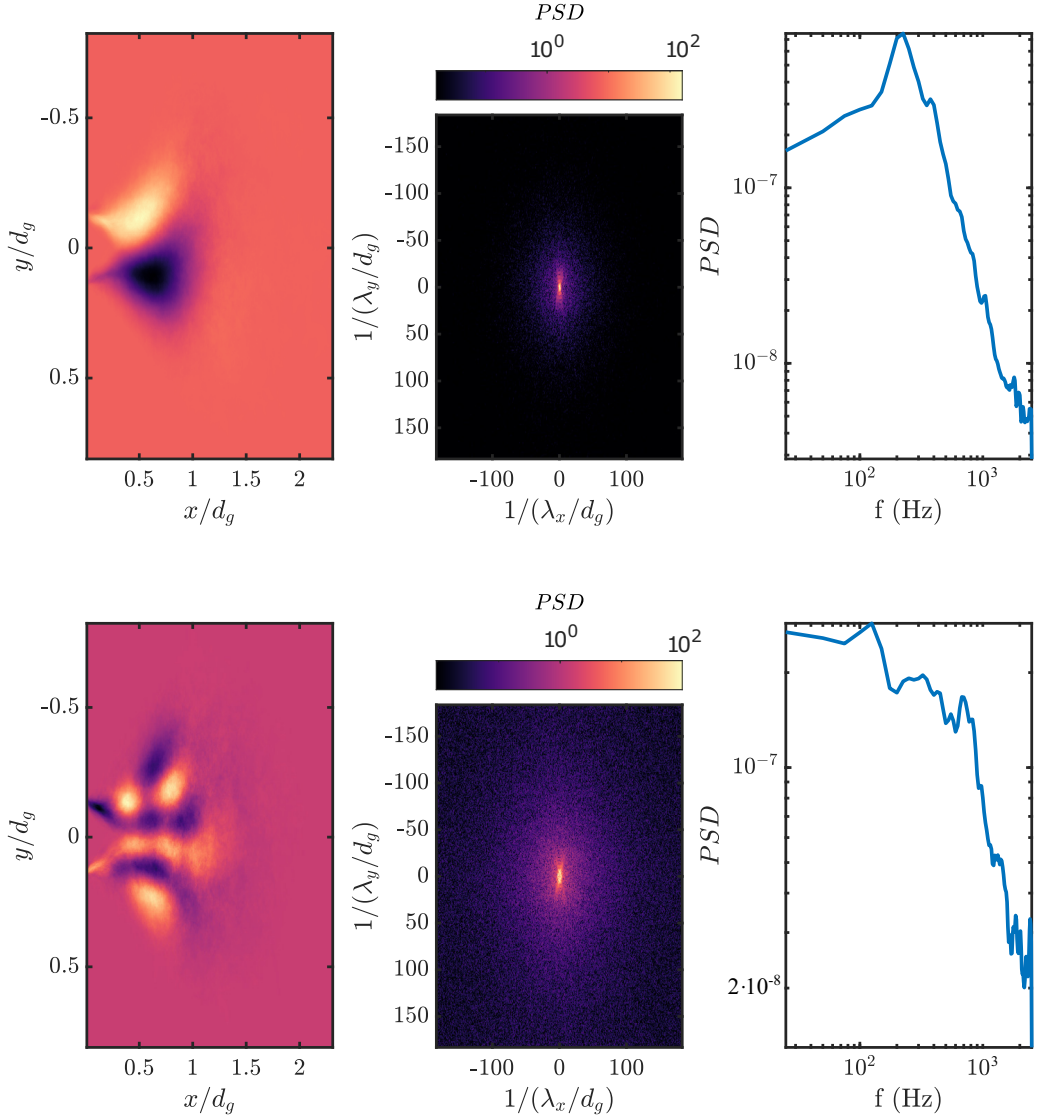


FIG. 4. POD modes (left), shown along with their two-dimensional fast Fourier transform (FFT) (middle) and the FFT of the corresponding time vector (right) for modes 1 (top) and 22 (bottom). Higher-order modes contain shorter wavelengths in space and higher frequencies in time.

### III. RESULTS

#### A. Liquid core lengths

Figure 5 shows snapshots of atomization at three-momentum ratios with (right) and without (left) electric field. The snapshots show the electrostatic effect for the electric field with a stronger axial component attained for the charged plates configuration. The influence of the electric field is readily apparent in the increased curvature and decreased intact length of the liquid core.

The axial electric field results in significantly shorter intact lengths at all momentum ratios explored, as opposed to the radial electric field that leaves the intact length approximately unchanged (Fig. 6). The mean liquid core length reveals the same trend as the intact length, indicating a clear

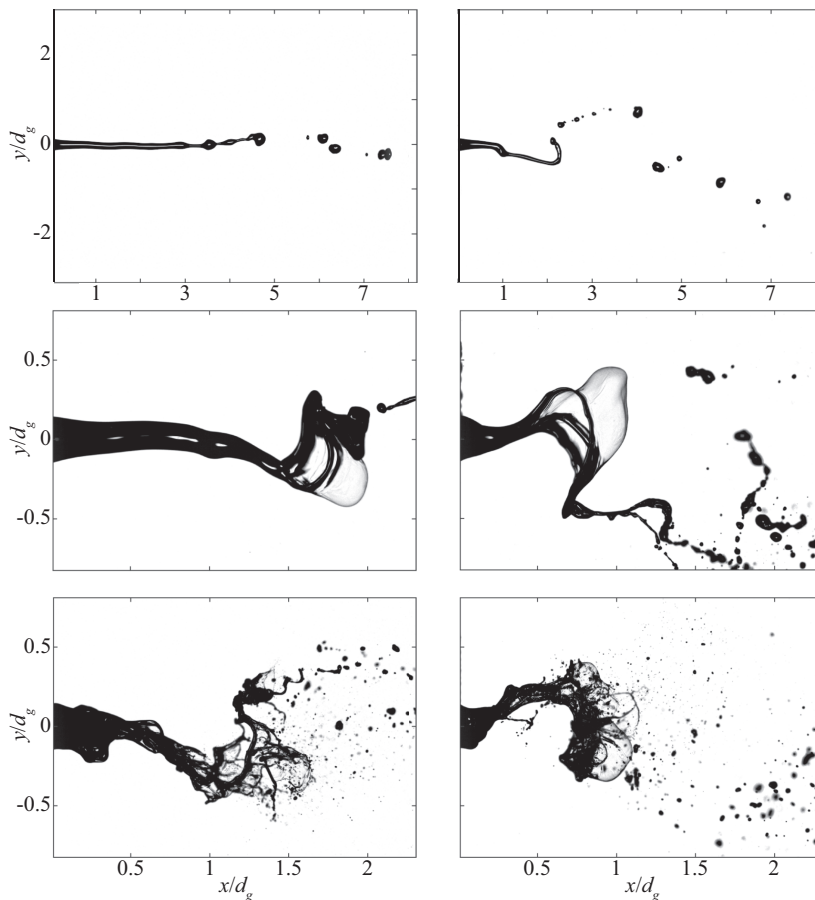


FIG. 5. Snapshots of the liquid core at momentum ratios of 1, 2, and 5 ( $U_g = 15, 23, 35$  m/s), with no electric field,  $Eu = 0$  (left), and with the axially oriented electric field,  $Eu = 10^{-2}$  (right), attained in the charged plate configuration. Notice the higher curvature and shorter intact length for the case with the electric field.

reduction due to the axial electric field across all momentum ratios explored (Fig. 6). For the case of the radial electric field, there is a smaller reduction in the liquid core length for the two smallest momentum ratios. The observed liquid core lengths (especially at low  $M$ ) are in good agreement with the expression derived by Lasheras and Hopfinger [10]:

$$\frac{L_c}{d_l} \approx \frac{6}{\sqrt{M}} \left( \left| 1 - \frac{U_l}{U_g} \right| \right)^{-1}. \quad (2)$$

Interestingly, Fig. 7 shows that the standard deviation of the liquid length remains relatively unaffected by the electric field, whereas the skewness is strongly affected by the axial electric field. All the values of the kurtosis are close to 3 (the kurtosis of a normal distribution), indicating that the distributions do not have very broad tails (Fig. 7).

In addition to the intact length, we characterized the mean liquid cone geometry in terms of the spreading angle and virtual origin (Fig. 8). For low momentum ratios, enhanced atomization, due to the axial electric field, leads to a much larger spreading angle. In contrast, for larger momentum ratios, the spreading angle is noticeably smaller whenever the electrostatic forces tend to repel the

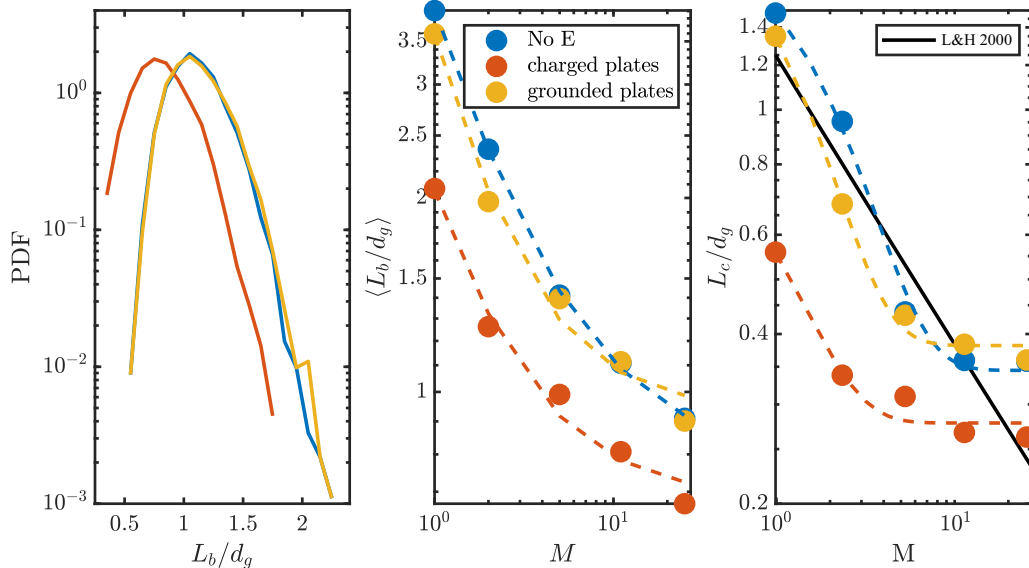


FIG. 6. Left: Probability density function (PDF) of intact length for  $M = 11$ . Only the radial electric field has a substantial effect in reducing the intact length. Middle: Mean intact length as a function of momentum ratio. Dashed lines are power laws fits, displaced by a constant. Right: Liquid core length as a function of  $M$ . The black line is the expression proposed by Lasheras and Hopfinger [10]. The fits are all exponentials plus a constant with  $R^2 > 0.95$ .

droplets away from the plates (i.e., for the case when the plates are held at the same potential as the liquid nozzle).

### B. Liquid core frequencies

We measured two key aspects (and their corresponding frequencies) of the liquid motion that are critical to understanding the breakup dynamics: the flapping frequency and the shedding frequency. The flapping frequency can be detected by the transversal variations of the light intensity in the liquid core region, whereas the shedding frequency can be identified from the time series of the intact length. Determination of these frequencies from the power spectra of the aforementioned time series was described in detail in previous work [24,28]. As shown in Fig. 9, no significant impact of the electrostatic field or the droplets' electric charge on the flapping frequency was observed. In contrast to the flapping frequency, the shedding frequency does get modified by the electrostatic forcing (Fig. 9). The shedding frequency was observed to increase for all momentum ratios due to electrostatic forcing in the grounded plates configuration (predominantly radial electric field).

The ratio of the shedding to the flapping frequency decreases as a function of momentum ratio, and it appears to have an asymptotic value of one half. This reveals a differential effect of the hydrodynamic instabilities of the liquid-gas interface on the shedding dynamics and, consequently, on the intermittency of the droplet generation. Furthermore, the characteristic frequencies computed from the time series of the number of drops crossing the edge of the image, shown in the bottom left panel of Fig. 9, matched well with the liquid core shedding frequency.

### C. Empirical dispersion relations

In order to investigate whether the electrostatic forcing modified the dynamics of smaller-scale features of the primary breakup, we computed empirical dispersion relations (Fig. 10). As expected for all the conditions, longer wavelengths (smaller wave numbers) corresponded to lower

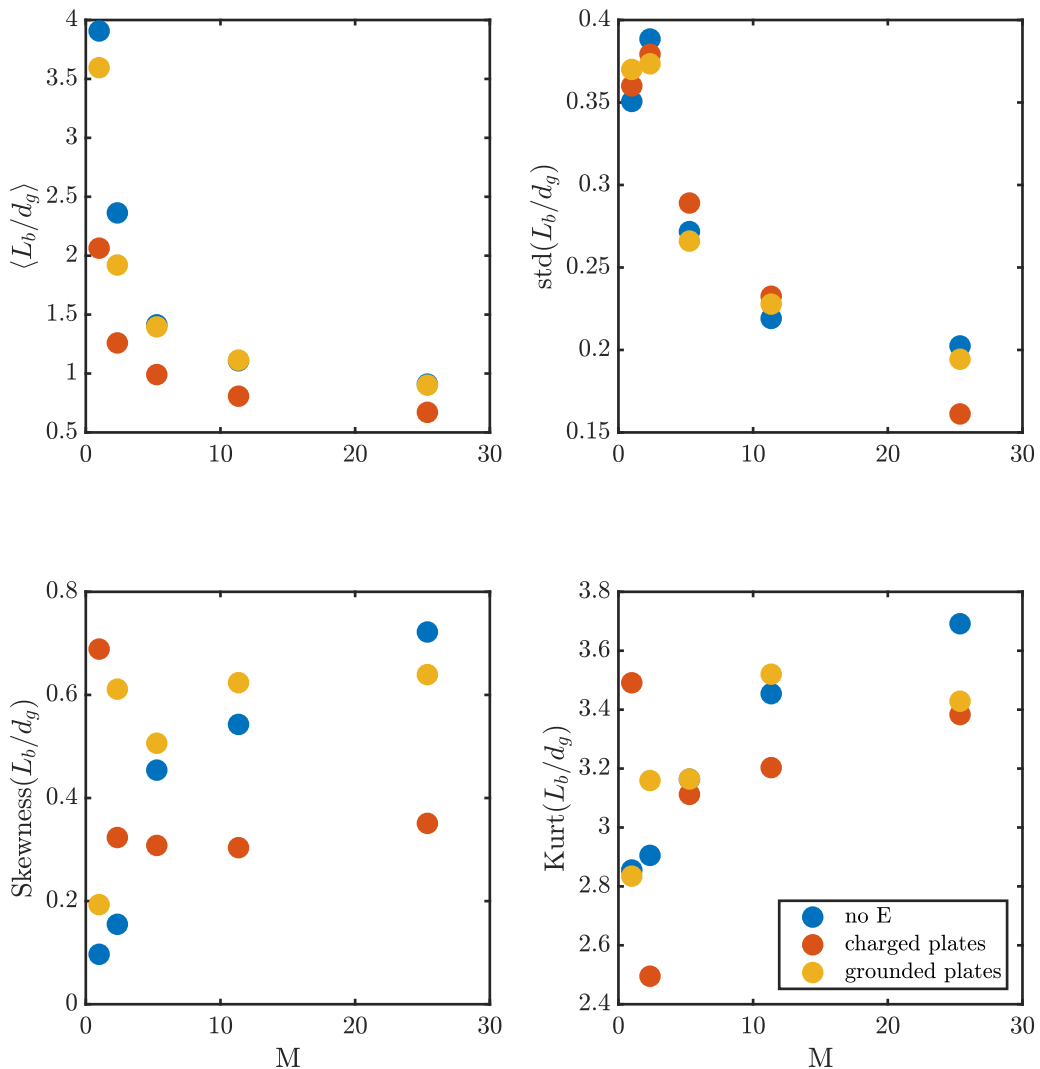


FIG. 7. First four statistical moments of the liquid intact length.

frequencies. More interestingly, the empirical dispersion relations clearly captured the faster dynamics prevalent at all length scales as the momentum ratio increased. Moreover, for a momentum ratio of 1, the empirical dispersion relation did reveal that the axial electric field resulted in faster dynamics at smaller scales. However, at higher momentum ratios, no configuration of the electric field resulted in noticeable changes in the dispersion relations.

#### D. Initial interfacial instabilities

Along with the global characterizations of the spray, we explored the dynamics of the initial interfacial disturbances by tracking their position to evaluate their velocities, as well as their characteristic wavelengths. The entrainment velocity clearly increases with momentum ratio but appears unaffected by the electric field (Fig. 11). The entrainment velocity was observed to be proportional to the square root of the momentum ratio, consistent with the work of Villermaux and coauthors [25,26], where  $u_e \approx \lambda \dot{\xi} / \xi \propto U_g$ .



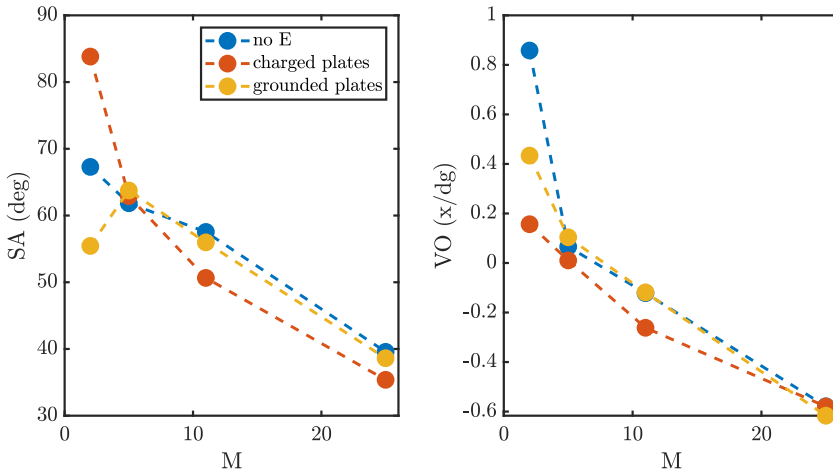


FIG. 8. Spreading angle and virtual origin.

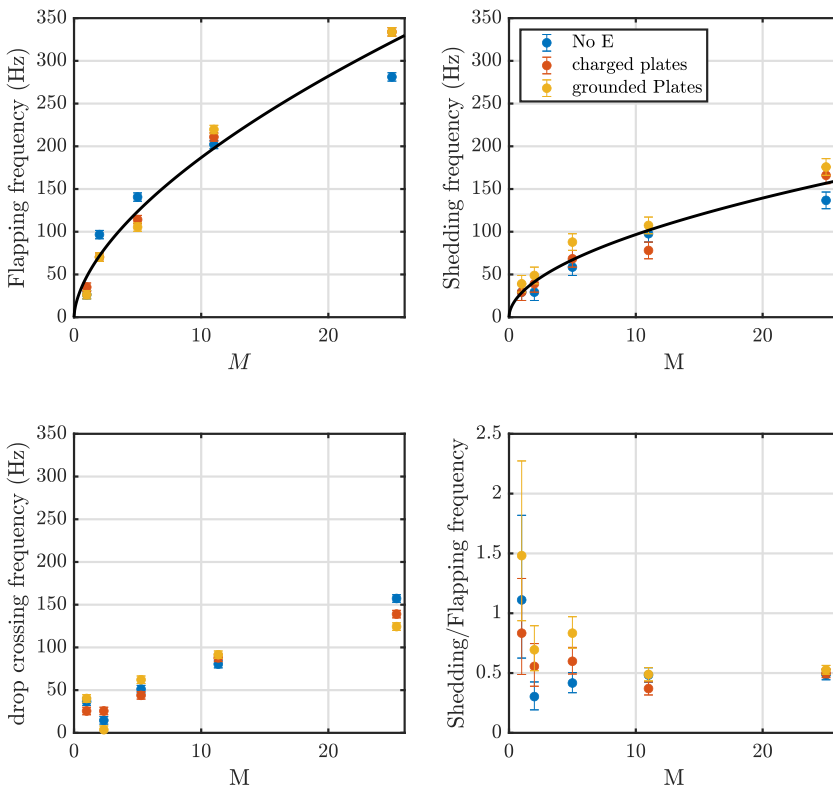


FIG. 9. Flapping (top left), shedding (top right), and drop crossing (bottom left) frequencies as a function of momentum ratio. Error bars indicate the spectral resolution of the Fourier transform used to compute Welch's power spectral density estimate. The ratio of the shedding to the flapping frequency (bottom right) decreases as a function of the momentum ratio to an asymptotic value of 0.5 (error bars in the ratios are derived from the error bars in the frequencies).

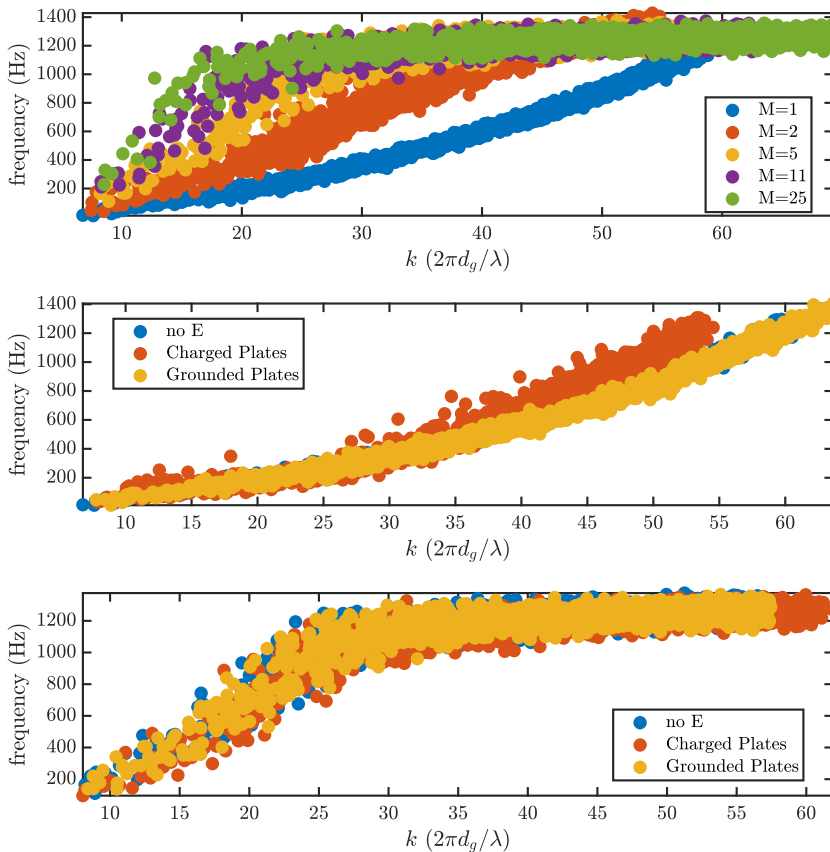


FIG. 10. Empirical dispersion relation as a function of  $M$  (top) and electric field for  $M = 1$  (middle) and  $M = 5$  (bottom).

In contrast, the wavelength of these interfacial disturbances follows the same trend as the core length, with the charged plates configurations exhibiting systematically shorter wavelengths than the other two configurations. These two trends result in estimated growth rates that are always faster in the presence of the axial electric field.

### E. Droplet population characterization

Finally, we performed optical identification of drop sizes in order to compute drop size distributions. As seen in Fig. 12, there are small differences in the tails of the mean diameter distributions, indicating a smaller fraction of large drops in the presence of the axial electric field. The differences in the volume-weighted distributions are more noticeable and clearly show that smaller drops are a larger proportion of the total spray volume flux for the axial electric field case.

The small difference in the arithmetic drop distribution seen above was observed through most experimental conditions (except at the lowest momentum ratio) and can be expressed in terms of the arithmetic mean diameter (Fig. 13). Higher moments of the drop size distribution, however, were smaller in the presence of the axial electric field compared with the other two configurations. In particular, the  $d_{43}$  values for the radial and axial electric field configurations were about 2% and 14% smaller than the values without electrostatic forcing, respectively, over the whole range of  $M$  explored here.

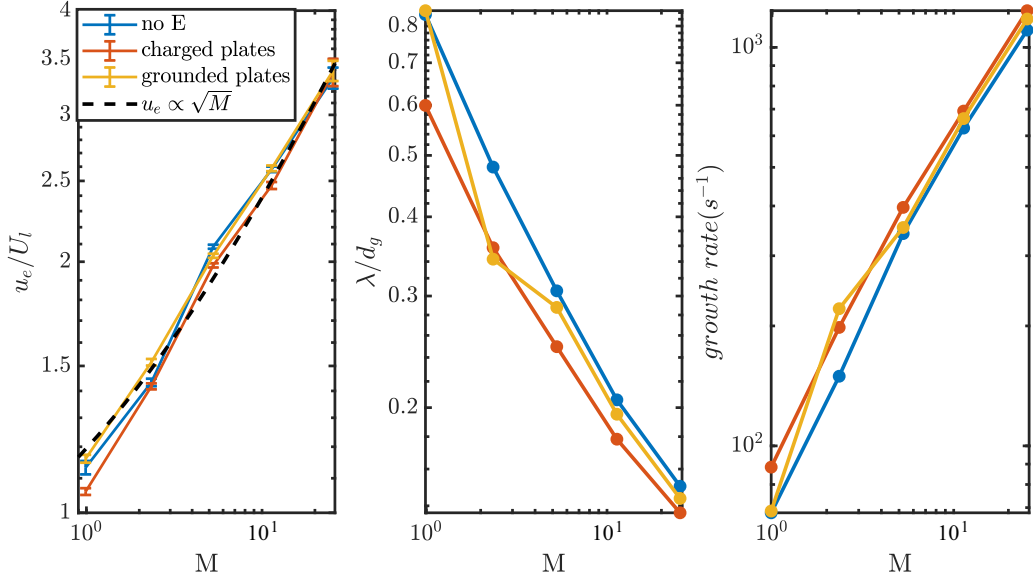


FIG. 11. Entrainment velocity normalized by the mean liquid injection velocity  $U_l$  along with a linear fit to the square root of the momentum ratio (left), wavelength of interfacial disturbances (middle), and growth rate of disturbances (right). The error bars are the standard error of the mean.

#### IV. DISCUSSION

Observations of the liquid core dynamics of coaxial atomization under electric field revealed that electric fields can significantly alter the wavelength and growth rate of interfacial instabilities, as

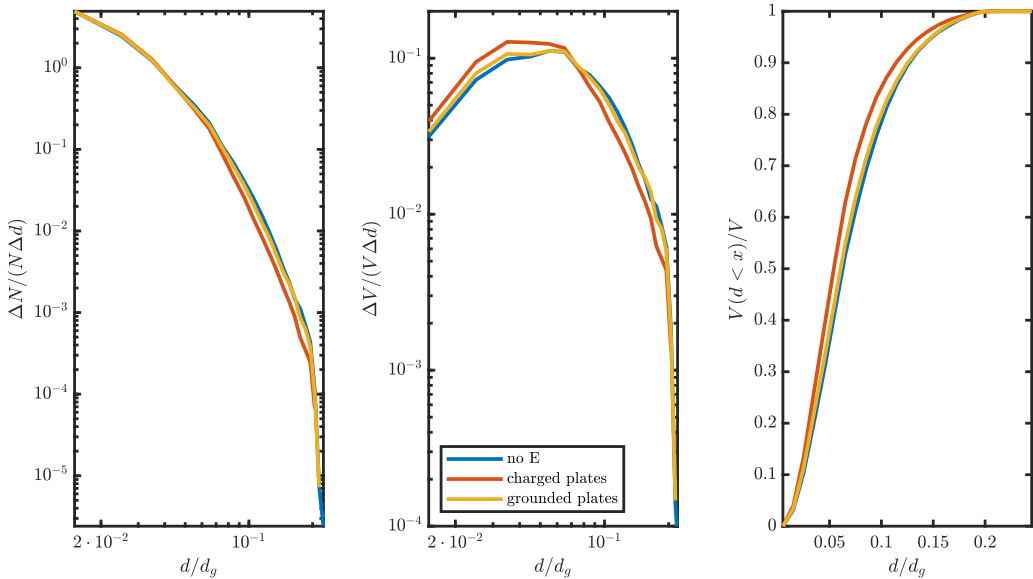


FIG. 12. Drop size distributions for the three configurations at a momentum ratio of 5. Arithmetic drop diameter distribution (left), volume-weighted distribution (center), and volume-weighted cumulative distribution (right).

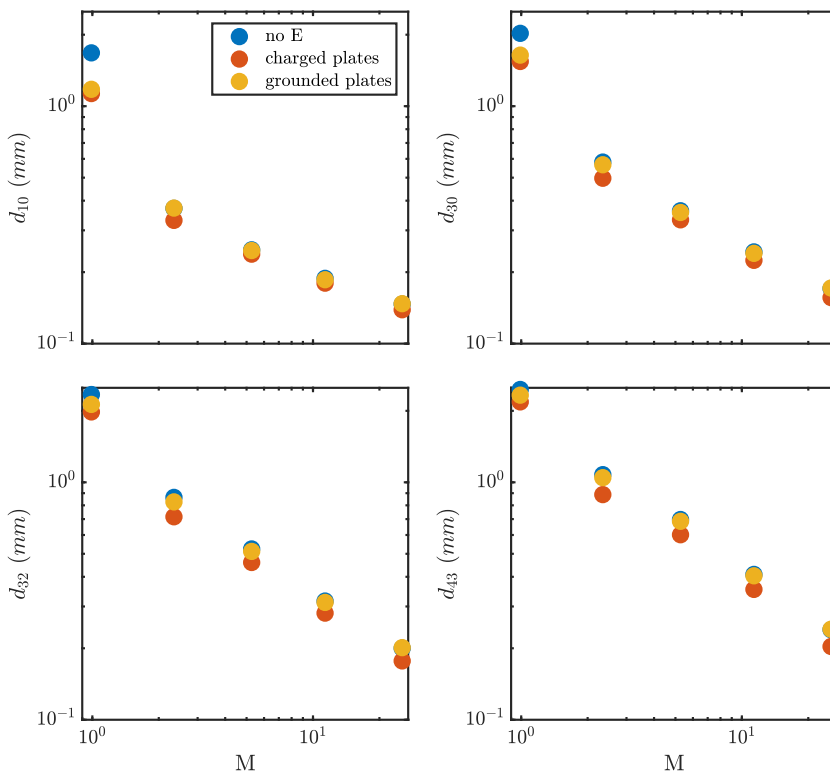


FIG. 13. Drop mean diameters:  $d_{10}$ , arithmetic mean diameter (top left);  $d_{30}$ , volume mean diameter (top right);  $d_{32}$ , Sauter (area-weighted) mean diameter (bottom left); and  $d_{43}$ , De Brouckere (volume-weighted) mean diameter (bottom right).

well as notably shorten the liquid core lengths and reduce the mean drop diameters. This effect was observed to persist up to much higher momentum ratios than had been explored before in electrostatic atomization, where the ratio of electrostatic to aerodynamic forces (as estimated from the electrical Euler number and the momentum ratio) was well below unity (about  $10^{-3}$ ). These observations are consistent with linear stability analysis in the literature [12], in which an electric field in the presence of surface charge increases the growth rate and shortens the wavelength of the interfacial instabilities.

The entrainment velocity of the interfacial corrugations was observed to be proportional to the gas velocity, in agreement with the theory developed by Villermaux and coauthors [25,26]. Interestingly, the entrainment velocity appeared to be unaffected by the electrostatic forcing. This suggests that the axial acceleration of interfacial corrugations was dominated by the aerodynamic stresses, a result that is consistent with the small ratio of Euler number to momentum ratio.

Moreover, the enhanced growth rate and shorter characteristic wavelengths of the interfacial instabilities due to electrostatic forcing showed a strong dependence on the electric field geometry for similar field strengths. Notably, an electric field with a stronger axial component (and resulting electrostatic stresses in a direction opposite the flow) resulted in a greater enhancement of the interfacial instability growth rate and reduction of their wavelengths. A substantial shortening of the liquid core length consistent with the enhanced growth rate of the instabilities was also observed.

Pertaining to the initial growth of interfacial instabilities, a shortcoming of the present work is that helical modes cannot be adequately characterized by two-dimensional shadowgraphy data.

As indicated by earlier work [12,13], electrostatically assisted coaxial atomization presents strong helical modes in addition to the axisymmetric ones.

In contrast to what was observed for the initial interfacial instabilities and liquid core lengths, some of the more global metrics reveal little impact of the electrostatic forcing on the primary breakup dynamics. In particular, there was no discernible effect of the electrostatic forcing on the flapping frequencies or on the characteristic frequency of the drop crossing times. A slight increase in the shedding frequency was observed for all momentum ratios under the effect of the predominantly radial electric field. This is hypothesized to be caused by enhanced radial acceleration of the liquid core, resulting in faster ligament shedding. Moreover, while the empirical dispersion relations clearly separate the dynamics for different momentum ratios, they show noticeable change only under the axial electric field at very low momentum ratios (of order unity). These observations suggest that the overall breakup dynamics are still dominated by aerodynamic forces.

A sizable reduction in the mean drop diameters was observed under the axial electric field configuration. In particular, the reduction of the mean droplet diameter was largest for the higher moments of the distribution (volume weighted or volumetric flux weighted), indicating a difference caused by the electric field in the reduction of the largest drops formed by inefficient aerodynamic atomization. The histograms of the droplet diameter clearly confirm this effect: a deficit in the number of the largest drops in the distributions. As shown by earlier work [7], the mean diameter of the resulting droplet population is proportional to the wavelength of the interfacial instabilities, a conclusion consistent with the observations presented in this work. The increase in the growth rate of the surface instabilities due to Maxwell's stresses along with the unaffected entrainment velocity results in smaller structures that detach from the liquid core at a higher frequency; this, in turn, results in a reduction of the droplet size in the ensuing spray.

## V. CONCLUSIONS

Electrostatic forcing is shown to noticeably impact the primary atomization in a coaxial atomizer, especially if the electric field is predominantly axial at the liquid nozzle exit. Our observations are consistent with the presence of Maxwell's stresses that accelerate the liquid jet towards the turbulent gas stream, which would lead to an increased efficiency in the kinetic energy transfer from the gas and the liquid. Furthermore, these effects persist at higher momentum ratios than had been studied in the past. The Maxwell stresses, resulting from an electric field with a strong axial component, were observed to shorten the wavelength of the interfacial instabilities, leading to shorter liquid core lengths and smaller droplet diameters. In contrast, an electric field with a radial component with a similar strength but smaller axial component did not have such an impact on the length scale of the interfacial instabilities. More research is necessary to optimize the electric field characteristics that maximize the mechanical coupling between the phases for improved atomization.

## ACKNOWLEDGMENTS

This work was sponsored by the Office of Naval Research (ONR) as part of the Multidisciplinary University Research Initiatives (MURI) Program, under Grant No. N00014-16-1-2617. The views and conclusions contained herein are those of only the authors and should not be interpreted as representing those of ONR, the U.S. Navy, or the U.S. Government.

- 
- [1] M. Arai, The possibility of active attitude control for fuel spray, *Engineering* **5**, 519 (2019).  
[2] S. Murugappan, S. Acharya, D. C. Allgood, S. Park, A. M. Annaswamy, and A. F. Ghoniem, Optimal control of a swirl-stabilized spray combustor using system identification approach, *Combust. Sci. Technol.* **175**, 55 (2003).

- [3] R. Osuna-Orozco, N. Machicoane, P. D. Huck, and A. Aliseda, Feedback control of coaxial atomization based on the spray liquid distribution, *Atomization Sprays* **29**, 545 (2019).
- [4] R. Osuna-Orozco, N. Machicoane, P. D. Huck, and A. Aliseda, Feedback control of the spray liquid distribution of electrostatically assisted coaxial atomization, *Atomization Sprays* **30**, 1 (2020).
- [5] J. Eggers and E. Villermaux, Physics of liquid jets, *Rep. Prog. Phys.* **71**, 036601 (2008).
- [6] J. Grace and J. Marijnissen, A review of liquid atomization by electrical means, *J. Aerosol Sci.* **25**, 1005 (1994).
- [7] A. Aliseda, E. Hopfinger, J. Lasheras, D. Kremer, A. Berchielli, and E. Connolly, Atomization of viscous and non-Newtonian liquids by a coaxial, high-speed gas jet. Experiments and droplet size modeling, *Int. J. Multiphase Flow* **34**, 161 (2008).
- [8] A. Kumar and S. Sahu, Liquid jet breakup unsteadiness in a coaxial air-blast atomizer, *Int. J. Spray Combust. Dyn.* **10**, 211 (2018).
- [9] J. C. Lasheras, E. Villermaux, and E. J. Hopfinger, Break-up and atomization of a round water jet by a high-speed annular air jet, *J. Fluid Mech.* **357**, 351 (1998).
- [10] J. C. Lasheras and E. J. Hopfinger, Liquid jet instability and atomization in a coaxial gas stream, *Annu. Rev. Fluid Mech.* **32**, 275 (2000).
- [11] C. Dumouchel, On the experimental investigation on primary atomization of liquid streams, *Exp. Fluids* **45**, 371 (2008).
- [12] G. Li, X. Luo, T. Si, and R. X. Xu, Temporal instability of coflowing liquid-gas jets under an electric field, *Phys. Fluids* **26**, 054101 (2014).
- [13] T. Si, F. Li, X. Y. Yin, and X. Z. Yi, Modes in flow focusing and instability of coaxial liquid-gas jets, *J. Fluid Mech.* **629**, 1 (2009).
- [14] A. M. Gañán-Calvo, J. M. López-Herrera, and P. Riesco-Chueca, The combination of electrospray and flow focusing, *J. Fluid Mech.* **566**, 421 (2006).
- [15] A. M. Gañán-Calvo, Electro-Flow Focusing: The High-Conductivity Low-Viscosity Limit, *Phys. Rev. Lett.* **98**, 134503 (2007).
- [16] T. P. Forbes, T. M. Brewer, and G. Gillen, Primary and secondary droplet and charge transmission characteristics of desorption electro-flow focusing ionization, *Appl. Phys. Lett.* **102**, 214102 (2013).
- [17] T. P. Forbes and E. Sisco, Mass spectrometry detection and imaging of inorganic and organic explosive device signatures using desorption electro-flow focusing ionization, *Anal. Chem.* **86**, 7788 (2014).
- [18] E. Castro-Hernández, P. García-Sánchez, J. Alzaga-Gimeno, S. H. Tan, J. C. Baret, and A. Ramos, AC electrified jets in a flow-focusing device: Jet length scaling, *Biomicrofluidics* **10**, 043504 (2016).
- [19] P. He, H. Kim, D. Luo, M. Marquez, and Z. Cheng, Low-frequency ac electro-flow-focusing microfluidic emulsification, *Appl. Phys. Lett.* **96**, 174103 (2010).
- [20] N. Vilanova, V. R. Gundabala, and A. Fernandez-Nieves, Drop size control in electro-coflow, *Appl. Phys. Lett.* **99**, 021910 (2011).
- [21] E. Allaf-Akbari and N. Ashgriz, An electrospray in a gaseous crossflow, *J. Aerosol Sci.* **114**, 233 (2017).
- [22] The atomizer design is available to the community at <http://depts.washington.edu/fluidlab/nozzle.shtml>.
- [23] N. Machicoane, J. K. Bothell, D. Li, T. B. Morgan, T. J. Heindel, A. L. Kastengren, and A. Aliseda, Synchrotron radiography characterization of the liquid core dynamics in a canonical two-fluid coaxial atomizer, *Int. J. Multiphase Flow* **115**, 1 (2019).
- [24] N. Machicoane, G. Ricard, R. Osuna-Orozco, P. D. Huck, and A. Aliseda, Influence of steady and oscillating swirl on the near-field spray characteristics in a two-fluid coaxial atomizer, *Int. J. Multiphase Flow* **129**, 103318 (2020).
- [25] E. Villermaux, Mixing and spray formation in coaxial jets, *J. Propul. Power* **14**, 807 (1998).
- [26] E. Villermaux and H. Rehab, Mixing in coaxial jets, *J. Fluid Mech.* **425**, 161 (2000).
- [27] G. Ricard, N. Machicoane, R. Osuna-Orozco, P. D. Huck, and A. Aliseda, Role of convective acceleration in the interfacial instability of liquid-gas coaxial jets, *Phys. Rev. Fluids* **6**, 084302 (2021).
- [28] M. Kaczmarek, R. Osuna-Orozco, P. D. Huck, A. Aliseda, and N. Machicoane, Spatial characterization of the flapping instability of a laminar liquid jet fragmented by a swirled gas co-flow, *Int. J. Multiphase Flow* **152**, 104056 (2022).